Mathematics

https://www.aimspress.com/journal/Math

AIMS Mathematics, 11(1): 881–906.
DOI: 10.3934/math.2026038
Received: 27 October 2025
Revised: 04 December 2025
Accepted: 12 December 2025
Published: 12 January 2026

Research article

Application of Tri-layered RNN scheme for Maxwell model subject to MHD

Sana Ullah Saqib[1], Yin-Tzer Shih[1,*], Muhammad Jahanzaib[1], Abdul Wahab[2], Adnan[3] and Shih-Hau Fang[4,5]

[1] Department of Applied Mathematics, National Chung Hsing University, Taichung 40227, Taiwan
[2] Department of Mathematics, King Fahd University of Petroleum and Minerals (KFUPM), Dhahran 31261, Saudi Arabia
[3] Department of Mathematics, Mohi-ud-Din Islamic University, Nerian Sharif, AJ&K 12080, Pakistan
[4] Department of Electrical Engineering, National Taiwan Normal University, Taipei 106308, Taiwan
[5] Yuan Ze University, Taoyuan 320, Taiwan

***Correspondence:** Email: yintzer_shih@email.nchu.edu.tw ; Tel: +886422853459; Fax: +886422873028.

Abstract: This study examines the characteristics of the Maxwell model under the influence of magnetohydrodynamics (MHD). Due to its inherent viscosity and elasticity, this model has significant applications in both industrial and biological contexts. The core innovation of this work lies in the development and application of a soft computational approach, specifically, the design and implementation of layered supervised recurrent neural networks optimized via the Levenberg–Marquardt (LSRNNs-LMO) technique, to predict the thermodynamic properties of the Maxwell model over a sheet, with particular focus on melting heat and zero mass flux boundary conditions, as inspired by the Cattaneo-Christov heat flux formulation and Lorentz force effects (TMS-MHZCL) model. The LSRNNs-LMO model is trained using data generated through a reliable numerical scheme. Simulation outcomes from the proposed LSRNNs-LMO method show excellent agreement with numerical results across multiple test cases, exhibiting minimal errors and high robustness. The accuracy of the proposed technique is thoroughly validated using error histograms, optimization control curves (mean squared error), root-mean-square error, autocorrelation analysis, regression evaluation, and the Nash–Sutcliffe efficiency (NSE) metric for the TMS-MHZCL model. These assessments provide strong evidence of the predictive validity and precision of the developed LSRNNs-LMO approach.

Keywords: thermal properties of the Maxwell model; stretched sheet; Lobatto-IIIA scheme; Lorentz forces; magneto-hydrodynamics; recurrent neural network
Mathematics Subject Classification: 35A22, 76A02, 76A05, 76A20, 76D05, 76S05, 76W05

Abbreviations: LSRNNs-LMO: layered supervised recurrent neural network optimized via the Levenberg–Marquardt; TMS-MHZCL: thermodynamic properties of the Maxwell model over a sheet, with particular focus on melting heat and zero mass flux boundary conditions, as inspired by the Cattaneo-Christov heat flux formulation and Lorentz force effects; MSE: mean squared error; RMSE: root mean–square error; MAE: mean absolute error; MAPE: mean absolute percentage error; NSE: Nash–Sutcliffe efficiency.

Nomenclature

$\hat{T}_s$	Solid temperature	$(\hat{u},\hat{v})$	Velocity parameters
$\hat{k}$	Thermal conductivity	$\hat{T}_m$	Melting temperature
$\hat{C}_\infty$	Free stream concentration	$\hat{C}_s$	Heat capacity
θ	Temperature	$\hat{\rho}$	Fluid density
$\hat{\lambda}$	Relaxation time	$(\hat{x},\hat{y})$	Cartesian coordinate
$\hat{B}_0$	Magnetic field	$\hat{\psi}$	Stream function
$\hat{T}_\infty$	Free stream temperature	$\hat{D}_B$	Mass diffusion
$\hat{U}$	Velocity of the sheet	f	Dimensionless stream function
$\hat{\beta}$	Fluid parameter	φ	Dimensionless concentration
$\hat{\upsilon}$	Viscosity (kinematic)	$\hat{\mu}$	Viscosity (dynamic)
$\hat{\lambda}_1$	Latent heat	$\hat{C}$	Concentration
$\hat{M}$	Hartmann number	$\hat{a}$	Positive constant
$\hat{\sigma}$	Electrical conductivity	$\hat{C}_w$	Wall Concentration
$\hat{\eta}$	Similarity variable	Sc	Schmidt number

1. Introduction

Computational investigation has progressed across various phases, transitioning from scientific methods to model-based cognitive and mathematical analytical systems. We currently possess an overwhelming amount of data from many methodologies. The data-driven fourth approach has established novel methods and strategies to address the deficiencies of its conventional predecessors by formulating precise, discovery-oriented data mining techniques for extensive datasets. Current developments in computing technology, artificial intelligence (AI), data mining, and mathematical concepts have enhanced several traditional methods used in scientific advancements, including computer simulations, computational experimentation, and mathematical modeling.

In recent years, advances in computational methods for fluid studies have emerged from the integration of large datasets obtained from dynamic modeling, laboratory experiments, and field data. Numerous domains within computing, mathematics, and science are poised to standardize AI and its associated discipline, machine learning, by providing diverse methodologies for transforming data into knowledge through readily implementable software solutions. Numerous researchers have studied multiple fluid models using AI schemes. Thus, recurrent neural networks (RNNs) have diverse applications across numerous engineering and industrial domains [1–3].

Rapid advances in computing technology have led to greater computational power and speed. AI is increasingly influencing everyday life. Consequently, contemporary researchers and engineers are focusing more closely on AI. Deep neural networks are a practical approach to addressing poorly structured or unstructured work outcomes and are used worldwide. A powerful AI is predicated on the hypothesis that machines can embody prospective human conceptions through their capacity for reasoning. As a result, strong AI asserts that, in the near future, we will be surrounded by computers that exhibit human-like behavior and possess cognitive capabilities comparable to those of humans. This means these computers will be able to reason, think, and perform tasks that humans can. The debate over the feasibility of developing advanced artificial intelligence persists, despite current research being far from that goal.

Various forms of neural networks (NNs) can be used for distinct data formats, necessitating a selection based on the application. Long short-term memory (LSTM) models can learn and exploit temporal dependencies in the data. Furthermore, LSTMs leverage their internal memory, ensuring that forecasts depend on the most recent state of the input sequence rather than solely on the immediately supplied input. However, LSTM cannot be used in the proposed model because our simulation data lacks the long-range spatial information for which it is designed. Machine learning approaches have a notable ability to handle complex data trends, facilitating the efficient retrieval of relevant data and thereby accelerating the simulation process. Diverse computational and analytical techniques exist for addressing laminar boundary-layer flow problems; yet, the use of machine learning has significantly improved the examination and forecasting of boundary-layer flow by incorporating data-driven methods within the framework of fluid dynamics. That is why numerous investigations have focused on applying machine learning techniques to boundary-layer flow research.

Recently, RNNs have gained prominence as effective models for classification, pattern recognition, and forecasting across various fields. A large number of scientists and individuals are involved in diverse facets of the AI field, offering novel solutions. RNNs are proficient, productive, and effective at delivering high capacity for addressing complex problems across various domains. RNNs are skilled in addressing challenges across multiple sectors, including agriculture, healthcare, education, banking, administration, security, engineering, commodities trading, and the arts. Encompassing issues in manufacturing, transportation, cybersecurity, finance, insurance, property management, advertisement, power, and obstacles that exceed the computing capacity of established methodologies and conventional mathematics. The combination of RNNs with stochastic numerical solvers yields an efficient tool for addressing numerous complex problems, particularly those associated with differential equations. Recent developments in addressing flow problems through the integration of multiple domains and methodologies have been investigated in [4–6].

Fluid properties are crucial in numerous applications, including industrial processes, medical applications, polymer manufacturing, lubrication, and natural phenomena such as lava flows and blood circulation. Nanotechnology is increasingly significant across industries due to its numerous applications in the manufacture of power-control devices, automobiles, and healthcare products. Specifically, cooling mechanisms in microelectronic devices, hybrid fuel cells, solid-state lighting, high-powered engines, and biopharmaceutical processes. Numerous sectors require the rapid implementation of efficient cooling methods, owing to rapid advances in semiconductors in electronic and power transmission systems, as well as the need to dissipate heat from sources such as automotive engines. In several industrial applications, cooling is a paramount necessity and a challenging technological endeavor for engineers, due to the reliability and efficiency requirements of the diverse range of items that rely on it. The technology industry continues to face challenges in developing energy-efficient heat-transfer fluids for refrigeration because of their inherently low thermal conductivity. To address this issue and achieve improved thermal properties compared with conventional fluids such as oil, methyl ether, and water, nanoliquids are fabricated by incorporating nanoscale metallic particles to enhance the thermal and energy transport properties of energy-transfer fluids. When nanoscale particles are firmly maintained and uniformly dispersed in base liquids, their thermal characteristics are superior to those of conventional fluids. These liquids serve as advanced coolants, facilitating effective heat dissipation and mitigating thermal accumulation. Investigations into the application perspective, multiple domains, and parametric effects have been reported in the studies [7–9].

Many scientists and analysts have been motivated to examine the MHD flow of viscous fluids over a stretched surface due to their appealing thermo-physical properties, heat-transfer capabilities, and significant practical applications in everyday life. Numerous astronomical and geophysical phenomena have been investigated utilizing MHD. MHD examines the motion of a conducting fluid in a magnetic field, which governs its heating. Applications of MHD may include controlling nuclear power plants, MHD power sources, and metal sheet cooling, among others [10,11]. MHD has several applications in the industrial, medicinal, and petroleum industries, attracting the attention of researchers [12–14]. This discovery significantly enhanced our understanding of Maxwell fluid behavior in various situations.

The existing literature indicates that AI-driven application of a tri-layered RNN scheme has not yet been employed in the TMS-MHZCL model. The authors of the proposed study employed an LSRNN-LMO strategy to investigate the TMS-MHZCL model, yielding a more effective solution. This LSRNNs-LMO technique is unique and innovative, providing flexibility and efficient data processing, thereby enabling advances in tackling complex challenges in engineering and related domains. This enhances computational accuracy and allows the identification of viable solutions to industrial and technological challenges. The statistical analysis underscores the effectiveness of the LSRNN-LMO technique in addressing complex, nonlinear phenomena in fluid dynamics. The accuracy and reliability of the TMS-MHZCL mathematical model's outputs, together with the concept's clarity, robustness, seamless functionality, and adaptability, are essential characteristics. The research reveals that key approaches of artificial intelligence are used across numerous scientific and technical sectors. The unique features of the provided study are expressed as follows:

- The TMS-MHZCL model has been investigated using an advanced machine learning strategy designated layered supervised recurrent neural networks optimized by the Levenberg–Marquardt networks (LSRNNs-LMO) technique.
- The TMS-MHZCL model solution is examined through comprehensive training, testing, and validation processes.
- A sophisticated, intelligent computational approach, specifically the LSRNNs-LMO technique, has been employed to attain enhanced accuracy in the TMS-MHZCL model.
- MATLAB is utilized to generate the synthetic dataset for the LSRNNs-LMO approach by using the Lobatto-IIIA numerical method. The generated dataset has been used for the LSRNNs-LMO technique, offering a predicted result that is compared with the conventional solution. The proposed technique yields results consistent with the observed numerical outcomes and exhibits minimal error.
- The level of accuracy of the developed LSRNNs-LMO technique is meticulously verified through the examination of the distribution of error histograms, mean squared error, root-mean-square error, autocorrelation analysis, and regression analysis.

The remainder of the article is structured as follows: Section 2 presents the Mathematical framework of the TMS-MHZCL model and describes the flow problem; Section 3 addresses solution methodologies for the TMS-MHZCL model, emphasizing the numerical LSRNN-LMO strategy used to solve the governing equations; Section 4 presents the research findings and evaluation of the LSRNNs-LMO strategy, examining the impact of dimensionless factors on various flow parameters; and Section 5 succinctly summarizes the investigation, highlighting significant findings and offering closing observations on the system's effectiveness.

2. Mathematical modeling

We considered the thermodynamic properties of the Maxwell model, focusing on MHD and the Cattaneo–Christov model. The configuration is considered for a sheet in Cartesian coordinates. This involves a Maxwell fluid flowing and transferring energy within a continuous boundary layer toward a stretched horizontal surface while steadily melting into a uniformly heated liquid of identical nature, as illustrated in Figure 1. The velocity of the stretching surface is considered as $\hat{u} = \hat{U}_w = \hat{a}\hat{x}$, where $\hat{a}$ is a positive constant parameter associated with the stretching rate of the sheet. The surface temperature is expressed as $\hat{T}_w$, whereas the free stream temperature is defined as $\hat{T}_\infty$, under the condition $\hat{T}_w < \hat{T}_\infty$. It is assumed that the fluid above the sheet possesses weak electrical conductivity and is affected by a uniform transverse MHD field of strength B_0. The coordinate measured along the sheet's stretching direction is denoted by $\hat{x}$. Additional presumptions about the fluidic configuration are as follows:

- The magnetic field is orthogonal to the surface.
- The sheet is extended homogeneously.
- The fluid flow is laminar.
- The fluid is incompressible.
- The model is appropriate for streamlining flow.
- It does not apply to a turbulent flow region.

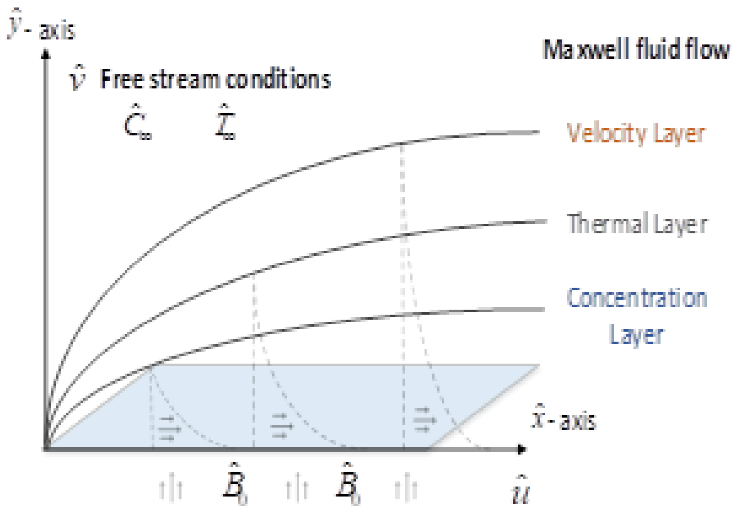

Figure 1. Problem geometry and flow.

Equation of continuity:

$$\hat{u}_x + \hat{v}_y = 0, \tag{1}$$

where the variables $\hat{u}_x$ and $\hat{v}_y$ represent the derivatives of the velocity parameters $\hat{u}$ and $\hat{v}$ with respect to the $\hat{x}$ and $\hat{y}$ directions, respectively. The momentum equation is defined as:

$$\hat{u}\hat{u}_x + \hat{v}\hat{u}_y + \hat{\lambda}\left[\hat{u}^2\hat{u}_{xx} + 2\hat{v}\hat{u}_{xy} + \hat{v}^2\hat{u}_{yy}\right] = \frac{\hat{\mu}}{\hat{\rho}}\hat{u}_{yy} - \frac{\hat{\sigma}\hat{B}_0^2}{\hat{\rho}}\hat{u}, \tag{2}$$

where relaxation time is denoted by $\hat{\lambda}$, fluid density by $\hat{\rho}$, kinematic viscosity by $\hat{\upsilon}$, electrical conductivity by $\hat{\sigma}$, and magnetic field by B_0.

A non-dimensional equation is obtained, as proposed by Yacob et al. [15], using the given similarity transformations and dimensionless measures.

$$\begin{aligned} &\hat{u} = \hat{a}\hat{x}f'(\xi), && \xi = \hat{y}\left(\frac{\hat{a}}{\hat{v}}\right)^{1/2}, && \hat{v} = -\sqrt{\hat{v}\hat{a}}\,f(\xi), \\ &\hat{\beta} = \hat{a}\hat{\lambda}, && \hat{M} = \frac{\hat{\sigma}\hat{B}_0^2}{\hat{\rho}}, && \psi = -\sqrt{\hat{v}\hat{a}}\,f(\xi)\hat{x}. \end{aligned} \tag{3}$$

The momentum equation describes fluid motion in Maxwell fluids, including the MHD effect, on a stretched sheet. It also accounts for magnetic field forces, viscosity, and elasticity. This formula is essential for comprehending how the stretched sheet changes fluid distribution and velocity.

$$\begin{aligned} &f''(\xi)f(\xi) - \hat{M}f'(\xi) - f'^2(\xi) + \hat{M}f'(\xi) + \\ &\qquad \hat{\beta}\left[-f^2(\xi)f'''(\xi) + 2f(\xi)f'(\xi)f''(\xi)\right] + f'''(\xi) = 0. \end{aligned} \tag{4}$$

In this case, *f* represents a non-dimensional stream function, and the prime notation represents differentiation with respect to ξ, $\hat{M}$ represents the magnetic field, and $\hat{\beta}$ signifies the Deborah number. References [16,17] provide details on the application of dimensional boundary conditions.

$$\begin{aligned} &\hat{u} = \hat{U}_w = \hat{a}\hat{x} \quad \text{at} \quad \hat{y} = 0, \\ &\hat{u} \to 0 \qquad\qquad \text{at} \quad \hat{y} \to \infty. \end{aligned} \tag{5}$$

So, the non-dimensional boundary conditions are:

$$\begin{aligned} &f = 1 \quad \text{at} \quad \xi = 0, \\ &f' = 0 \quad \text{at} \quad \xi \to \infty. \end{aligned} \tag{6}$$

The energy equations illustrate the transmission and distribution of thermal energy inside a fluidic system, which is crucial for fluid movement analysis. The Maxwell fluid, characterized by its distinctive viscoelastic properties, is described by the energy equation, which makes it particularly important. Usually, the equation includes parameters for heat sources or sinks, convection, and heat transport.

$$\hat{u}(\hat{T}_x) + \hat{v}(\hat{T}_y) = \frac{\hat{k}}{\hat{\rho}\hat{c}_p}(\hat{T}_{yy}). \tag{7}$$

Using non-dimensional quantities and similarity transformations, we will get a dimensionless equation:

$$\theta = \frac{\hat{T} - \hat{T}_m}{\hat{T}_\infty - \hat{T}_m}, \quad \hat{v} = -\sqrt{\hat{v}\hat{a}}\, f(\xi), \quad \hat{u} = \hat{a}\hat{x} f'(\xi), \quad Pr = \frac{\hat{v}}{\hat{a}}, \tag{8}$$

where $\hat{a}$ is the thermal diffusivity, θ represents the temperature profile, *Pr* is the dimensionless Prandtl number, and $\hat{T}$ is the temperature.

The internal thermal energy balance of the fluid is accounted for in the energy equation for the motion of a Maxwell fluid. It illustrates how heat is generated, transferred, and released as a fluid moves and interacts with its surrounding environment. The equation also accounts for the Maxwell fluid's viscoelastic nature, which has both elastic and viscous characteristics.

$$\theta''(\xi) + Pr\, f(\xi)\theta'(\xi) = 0. \tag{9}$$

Subject to the following boundary conditions:

$$\begin{aligned} &\hat{T} = \hat{T}_m \quad \text{at} \quad \hat{y} = 0, \\ &\hat{T} \to \hat{T}_\infty \quad \text{at} \quad \hat{y} \to \infty. \end{aligned} \tag{10}$$

So, the non-dimensional boundary conditions are:

$$\begin{aligned} &\theta = 0 \quad \text{at} \quad \xi = 0, \\ &\theta \to 1 \quad \text{at} \quad \xi \to \infty. \end{aligned} \tag{11}$$

The continuity equation, often called the mass conservation equation, is a fundamental principle of fluid mechanics and a mathematical expression of the law of conservation of mass. It describes how the fluid's density remains constant as it moves across a stretched sheet, thereby preserving mass conservation within the system.

$$\hat{u}\hat{C}_x + \hat{v}\hat{C}_y = \hat{D}_B \hat{C}_{yy} \ , \tag{12}$$

where $\hat{D}_B$ stands for mass diffusion and $\hat{C}$ for concentration. Using the non-dimensional values and similarity transformations given below, we will derive a dimensionless equation.

$$\varphi = \frac{\hat{C} - \hat{C}_\infty}{\hat{C}_w - \hat{C}_\infty}, \quad Sc = \frac{\hat{v}}{\hat{D}_B}, \tag{13}$$

where Sc is the dimensionless Schmidt number, and φ is the dimensionless concentration profile.

$$\varphi''(\xi) - Sc\, f(\xi)\varphi'(\xi) = 0. \tag{14}$$

The boundary conditions for zero mass flux are in effect when there is no transfer of mass across a barrier. The condition states that, if the total mass entering the border equals the mass leaving the border, the net mass transfer is zero, which can be expressed as follows.
The boundary conditions can be modeled as

$$\begin{aligned} &\hat{C} = 0 \quad &&\text{at} \quad \hat{y} = 0, \\ &\hat{C} \to \hat{C}_\infty \quad &&\text{at} \quad \hat{y} \to \infty. \end{aligned} \tag{15}$$

After applying similarity transformations, we are left with:

$$\begin{aligned} &\varphi = 0 \quad &&\text{at} \quad \xi = 0, \\ &\varphi' \to \infty \quad &&\text{at} \quad \xi \to \infty. \end{aligned} \tag{16}$$

3. Solution methodology: employ AI-driven, innovative computational techniques that integrate the LSRNNs-LMO strategy

The layered supervised recurrent neural networks optimized by the Levenberg-Marquardt method (LSRNN-LMO) concept has been developed as a novel approach for simulating and interpreting complex nonlinear fluid dynamics. The primary aim of this research is to optimize and simulate a hysteresis model of actuators using layered supervised recurrent neural networks (LSRNNs) in combination with local search Levenberg-Marquardt (LM) optimization.

The mathematical framework of recurrent neural networks is a nonlinear state-space model of the inherent dynamic behaviors. This characteristic of RNNs makes them well-suited to handling nonlinear and unstable flows. The proposed LSRNN-LMO technique captures the spatial and temporal aspects of the unstable fluid environment independently. The mathematical architecture of a nonlinear state-space standard recurrent neural network is represented as follows:

$$l_t = s(l_{t-1}, I_t + b),$$

$$l_t = ReLU(W_{ll}l_{t-1} + W_{Il}I_t + b),$$
$$Y_t = W_{ly}I_t. \tag{17}$$

Let t stand for the time interval, l_t signify the currently visible hidden state, l_{t-1} indicate the previous hidden state, I_t indicate the most recent input vector at time step t, s refer to the analogous (recurring) operation for every input, b represents the bias term during sequential computation of data, W_{ll} serve as the weight that existed at the prior hidden state, W_{ly} signify the weight at the currently visible input state, and Y_t signify the output.

The dimension of the vector from hidden to hidden is $W_{ll} \in R^{n\times n}$, and $W_{Il} \in R^{n\times m}$ is the input dimension of the weight vector. The bias component is $b \in R^n$. The proposed technique employs a nonlinear activation function known as rectified linear unit (ReLU). A linear transformation is applied on I_t to determine the output Y_t at each time step.

We have presented supervised deep-layered recurrent neural networks. This network can learn more complex patterns using deep RNNs, which enhance the fundamental architecture by stacking multiple recurrent layers. To improve the model's ability to accurately represent topological characteristics, the hidden states of each layer are passed to the next layer. The following is the most recent update of the hidden states at layer l and time step t for a deep LSRNN-LMO with l layers:

$$l_t{}^{(l)} = ReLU\left(W_{ll}{}^{(l)}l_{t-1}{}^{(l)} + W_{Il}{}^{(l)}I_t{}^{(l-1)} + b_l{}^{(l)}\right), \tag{18}$$

where $l_t{}^{(0)} = I_t$ denotes the input of the first layer. The procedure for computing the output at the highest level is identical to that of fundamental RNNs:

$$Y_t = ReLU\left(W_{Il}I_t{}^{(l)} + b_y{}^{(l)}\right). \tag{19}$$

Compared with shallow RNNs, deep RNNs can capture long-range dependencies and model complex patterns. We employed the ReLU nonlinear activation function for computational simulations of the (TMS-MHZCL) model. The network's ability to learn and comprehend sequences affects how it operates on specific tasks to achieve desired outcomes. The system (19) exemplifies a prototype of an LSRNN-LMO technique, featuring a feedback mechanism that demonstrates its capacity to learn from both contemporary and historical data.

RNNs are crucial for tasks that require modeling sequential data. RNNs are adept at processing large datasets with recurrent dependencies, leveraging sequential information from previous units. The RNN employs the number of initial function elements at the corresponding time step. The hidden phase is an inner status present in each of these elements. The hidden memory represents data from prior periods that the unit previously handled and stored at that specific time step. This initial state data is updated often at each time step, so it reflects the most current intelligence.

Multi-layer neural networks have been applied in learning frameworks because they can address nonlinear and complex decision-making problems. The design of the LSRNN-LMO strategy, which integrates 10 neurons in each hidden layer with a ReLU activation function, is illustrated in Figure 2(a). The TMS-MHZCL model's sequential dataset is generated using 100 input grids in the range [0, 1] for the LSRNN-LMO technique. Figure 2(b) illustrates the sequential workflow of the proposed LSRNN-LMO approach. The LSRNN-LMO output is generated using the MATLAB framework for a triple-layer recurrent neural network with LM optimization with backpropagation, as also described in Figure 2(b).

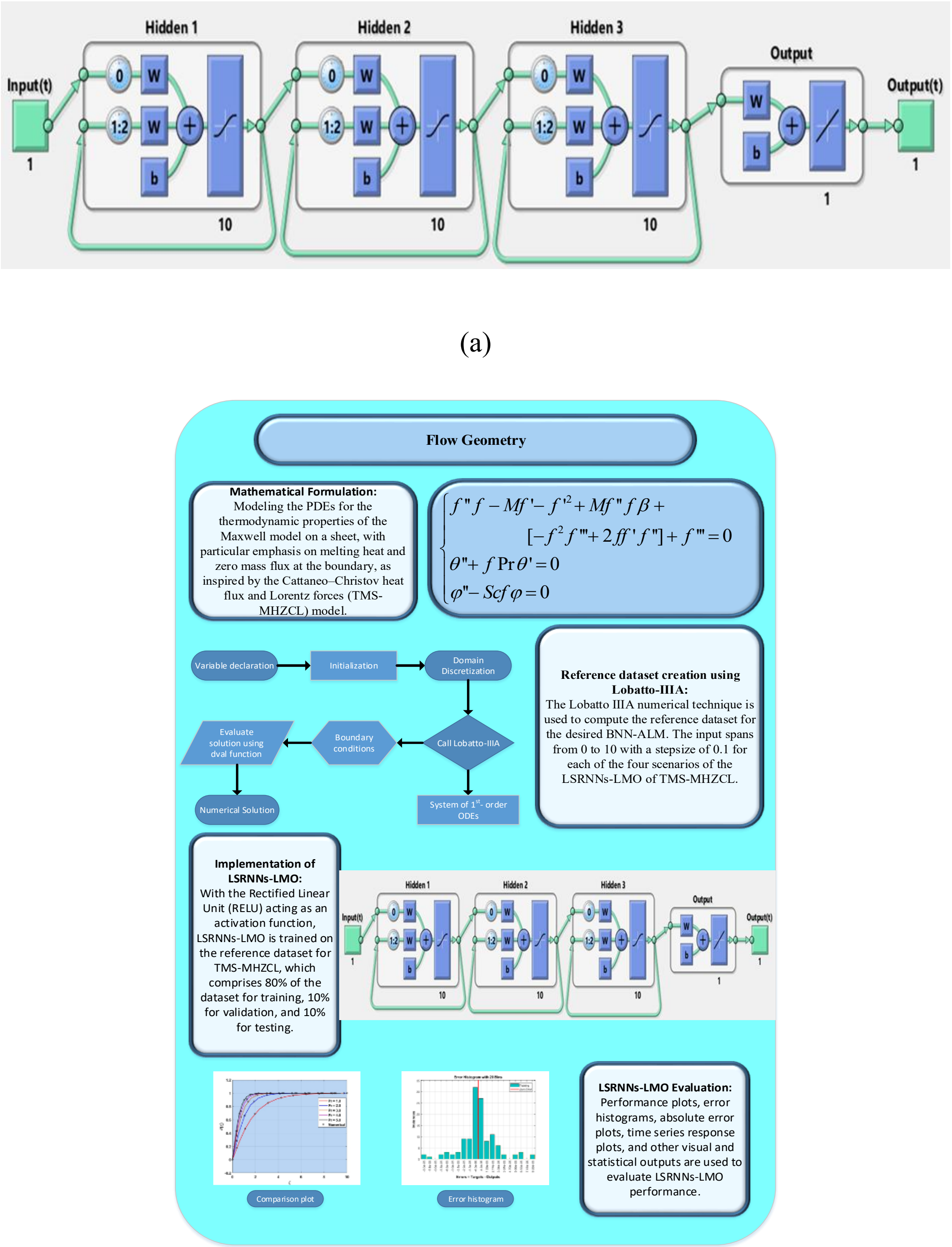

(a)

Flow Geometry

Mathematical Formulation: Modeling the PDEs for the thermodynamic properties of the Maxwell model on a sheet, with particular emphasis on melting heat and zero mass flux at the boundary, as inspired by the Cattaneo–Christov heat flux and Lorentz forces (TMS-MHZCL) model.

$$\begin{cases} f''f - Mf' - f'^2 + Mf''f\beta + \\ \qquad [-f^2 f''' + 2ff'f''] + f''' = 0 \\ \theta'' + f\,\mathrm{Pr}\,\theta' = 0 \\ \varphi'' - Scf\varphi = 0 \end{cases}$$

Reference dataset creation using Lobatto-IIIA: The Lobatto IIIA numerical technique is used to compute the reference dataset for the desired BNN-ALM. The input spans from 0 to 10 with a stepsize of 0.1 for each of the four scenarios of the LSRNNs-LMO of TMS-MHZCL.

Implementation of LSRNNs-LMO: With the Rectified Linear Unit (RELU) acting as an activation function, LSRNNs-LMO is trained on the reference dataset for TMS-MHZCL, which comprises 80% of the dataset for training, 10% for validation, and 10% for testing.

LSRNNs-LMO Evaluation: Performance plots, error histograms, absolute error plots, time series response plots, and other visual and statistical outputs are used to evaluate LSRNNs-LMO performance.

(b)

Figure 2. (a) Architecture of layered supervised recurrent neural networks; (b) Flow chart topology of the layered supervised recurrent neural networks technique.

An essential element in neural network development is selecting the activation function for neurons across multiple layers. Activation functions introduce nonlinearity into the mathematical representation of neural networks, enabling the network to gradually acquire improved feature representations. A variety of activation functions have been used in the scientific literature. Nonetheless, Tanh, linear, Sigmoid, and ReLU are among the most commonly used activation functions, typically selected empirically during network construction rather than through a systematic, data-driven approach. In this study, we employed the ReLU activation function. The ReLU activation function is defined as: $f(\xi) = \max(0, \xi)$. The ReLU activation function enables the network to learn intricate relationships in the data, resulting in reliable performance and accurate predictions when addressing complex problems. Figures 3–11 illustrate the remarkable efficacy of ReLU activation.

Different neural network architectures may operate on various types of data; therefore, it's essential to choose the right one for your needs. LSTMs can learn and exploit temporal dependencies in the data. LSTMs successfully capture long-term dependencies in sequential data, making them suitable for tasks such as speech recognition, language translation, and time-series forecasting. Moreover, LSTMs use their internal memory, ensuring that predictions rely on the most recent context in the input sequence rather than solely on the immediately preceding input. Unfortunately, LSTM cannot be applied to the TMS-MHZCL model due to constraints in our simulation data, as LSTM is designed for analyzing large-scale geographic data. Therefore, we implemented the SLSRNN-LMO methodology to solve the TMS-MHZCL model.

We employed 30 neurons per recurrent layer, with ReLU activation, to investigate the behavior of thermodynamic properties. Training is conducted utilizing the Adam optimizer with a learning rate of 0.001, a batch size of 64, and 1000 training epochs. The results were obtained using MATLAB Version R2018b on a PC. The obtained numerical results closely align with the reference outcomes. Computing simulation of the TMS-MHZCL model utilizing stochastic deep-layered recurrent neural networks (LSRNN-LMO) has not yet been implemented. The current research indicates that the TMS-MHZCL model has not been examined using the SLSRNN-LMO methodology. The uniqueness of this endeavor is evidenced by the absence of this advanced technique in the current scientific literature. This article introduces a novel method that integrates recent advances in SLSRNN-LMO into the TMS-MHZCL model. It can be used to address modeling issues in computational fluid mechanics applications, thereby improving the accuracy of flow and heat-transport predictions.

We employed a triple-layer recurrent neural network, utilizing LM optimization with backpropagation, as an innovative method for simulating and analyzing the complex, nonlinear dynamics of the TMS-MHZCL model. Investigations have revealed that deeper RNN architectures improve sequence modeling by capturing increasingly abstract representations across layers. This configuration demonstrated an effective balance between learning performance and computational efficiency in our assessments.

This study also describes the comprehensive approach employed to achieve its scientific objectives, including details on data collection and processing, the architectural design of LSRNN-LMO, optimization methodologies, network training, the experimental setup, and outcome evaluation metrics.

3.1 Metrics evaluation

This section describes the mathematical framework for the evaluation measurements that validate the accuracy of the layered supervised recurrent neural networks optimized by the Levenberg-Marquardt method (LSRNN-LMO), designed to address the thermodynamic properties of the Maxwell model on a sheet, with a specific focus on melting heat and zero mass flux at the boundary and relying inspiration from the Cattaneo-Christov heat flux and Lorentz forces (TMS-MHZCL) model. We rigorously analyze the efficacy of the proposed strategy using a range of statistical indicators. Convergence-based visual learning curves illustrate the training process and exhibit the model's ability to learn from the generated synthetic dataset. The MSE, RMSE, MAE, MAPE, NSE, and R² are statistical metrics that are used and presented as metrics used to evaluate cases of velocity, i.e., original or exact $f_e(\xi)$ and approximated or predicted $\hat{f}_p(\xi)$.

$$
\begin{aligned}
MSE &= \frac{1}{n}\sum_{j=1}^{n}\left(f_e(\xi_j) - \hat{f}_p(\xi_j)\right)^2, \\
RMSE &= \sqrt{\frac{1}{n}\sum_{j=1}^{n}\left(f_e(\xi_j) - \hat{f}_p(\xi_j)\right)^2}, \\
MAE &= \frac{1}{n}\sum_{j=1}^{n}\left|f_e(\xi_j) - \hat{f}_p(\xi_j)\right|, \\
R^2 &= \frac{\sum_{j=1}^{n}\left(f_e(\xi_j)-\frac{1}{n}\sum_{j=1}^{n}f_e(\xi_j)\right)\left(\hat{f}_p(\xi_j)-\frac{1}{n}\sum_{j=1}^{n}f_p(\xi_j)\right)}{\sqrt{\sum_{n-1}^{n}\left(f_e(\xi_j)-\frac{1}{n}\sum_{j=1}^{n}f_e(\xi_j)\right)^2\left(f_p(\xi_j)-\frac{1}{n}\sum_{j=1}^{n}\hat{f}_p(\xi_j)\right)^2}}.
\end{aligned}
\tag{20}
$$

Here, n represents the number of points on the grid.

These performance evaluation metrics play a crucial role in identifying prevailing trends and patterns related to the model's assessment accuracy, robustness, and predictive effectiveness under optimal conditions. The MSE, RMSE, MAE, MAPE, NSE, and R² effectively quantify the discrepancy between real and measured values. Optimal forecasting accuracy and its correspondence with real data are indicated by the predicted values of MAE, MSE, MAPE, RMSE, NSE, and R² at 0, 0, 0, and 1, respectively (see Tables 1 and 2), under optimal predictive conditions. Tables 1 and 2 illustrate the accuracy and efficiency of the proposed methodology.

Table 1. Results produced by the LSRNN-LMO procedure.

S=Scenario, C=Case	Performance (MSE)	Gradient	Time	Final iteration
S1/C1	2.25×10^{-13}	7.65×10^{-5}	35s	712
S1/C2	3.20×10^{-12}	4.12×10^{-6}	24s	620
S1/C3	1.68×10^{-12}	2.12×10^{-6}	28s	821
S1/C4	1.15×10^{-12}	1.15×10^{-7}	31s	715
S1/C5	2.60×10^{-13}	5.21×10^{-9}	25s	601
S2/C1	1.71×10^{-11}	2.16×10^{-4}	30s	412
S2/C2	3.12×10^{-13}	9.81×10^{-7}	25s	450
S2/C3	5.57×10^{-11}	1.89×10^{-8}	27s	412
S2/C4	2.77×10^{-13}	3.32×10^{-6}	20s	450
S2/C5	6.92×10^{-12}	6.16×10^{-8}	28s	550
S3/C1	3.77×10^{-13}	2.4×10^{-7}	28s	385
S3/C2	2.36×10^{-11}	3.30×10^{-9}	20s	412
S3/C3	4.11×10^{-13}	5.21×10^{-7}	32s	630
S3/C4	1.45×10^{-13}	9.66×10^{-8}	35s	725
S3/C5	7.45×10^{-11}	1.14×10^{-6}	30s	677
S4/C1	7.71×10^{-10}	4.08×10^{-8}	25s	1000
S4/C2	1.45×10^{-11}	5.44×10^{-7}	21s	880
S4/C3	3.19×10^{-10}	2.10×10^{-7}	30s	990
S4/C4	7.04×10^{-13}	8.18×10^{-8}	18s	752
S4/C5	1.10×10^{-12}	7.75×10^{-9}	20s	801

Table 2. Outcomes obtained by the LSRNN-LMO technique.

S=Scenario, C=Case	RMSE	MAE	MAPE	R^2	$1-R^2$
S1/C1	4.74×10^{-7}	2.13×10^{-7}	2.88×10^{-5}	0.99	1.66×10^{-13}
S1/C2	1.79×10^{-6}	3.05×10^{-7}	1.71×10^{-4}	0.99	3.54×10^{-13}
S1/C3	1.30×10^{-6}	1.28×10^{-6}	3.59×10^{-5}	0.99	2.95×10^{-12}
S1/C4	1.07×10^{-6}	1.02×10^{-6}	1.77×10^{-5}	0.99	1.50×10^{-12}
S1/C5	5.10×10^{-7}	2.98×10^{-7}	3.22×10^{-5}	0.99	5.90×10^{-12}
S2/C1	4.14×10^{-6}	1.23×10^{-7}	3.98×10^{-5}	0.99	2.22×10^{-13}
S2/C2	5.59×10^{-7}	1.01×10^{-7}	2.75×10^{-5}	0.99	1.06×10^{-13}
S2/C3	7.46×10^{-6}	1.17×10^{-6}	1.22×10^{-4}	0.99	5.19×10^{-12}
S2/C4	5.26×10^{-7}	1.57×10^{7}	1.22×10^{-5}	0.99	1.10×10^{-13}
S2/C5	2.63×10^{-6}	1.33×10^{-6}	5.66×10^{-5}	0.99	8.88×10^{-11}
S3/C1	6.14×10^{-7}	1.12×10^{-7}	1.77×10^{-5}	0.99	5.44×10^{-13}
S3/C2	4.86×10^{-6}	1.15×10^{-6}	2.70×10^{-4}	0.99	3.12×10^{-12}
S3/C3	6.41×10^{-7}	1.77×10^{-7}	1.12×10^{-5}	0.99	2.99×10^{-13}
S3/C4	3.81×10^{-7}	2.00×10^{-7}	3.09×10^{-5}	0.99	7.52×10^{-13}
S3/C5	8.63×10^{-6}	2.54×10^{-5}	1.14×10^{-5}	0.99	6.62×10^{-12}
S4/C1	2.77×10^{-5}	2.92×10^{-6}	3.88×10^{-4}	0.99	5.88×10^{-11}
S4/C2	3.81×10^{-6}	3.23×10^{-6}	1.50×10^{-4}	0.99	3.61×10^{-12}

Continued on next page

S=Scenario, C=Case	RMSE	MAE	MAPE	R^2	$1-R^2$
S4/C3	1.79×10^{-5}	1.22×10^{-6}	2.56×10^{-4}	0.99	2.33×10^{-11}
S4/C4	8.39×10^{-7}	1.25×10^{-6}	1.01×10^{-5}	0.99	6.11×10^{-13}
S4/C5	1.05×10^{-6}	3.88×10^{-6}	3.02×10^{-5}	0.99	4.55×10^{-11}

4. Results and discussion

This section is designed to clarify the results achieved through the application of the layered supervised recurrent neural networks with Levenberg-Marquardt optimization (LSRNNs-LMO) technique, to forecast the thermodynamic properties of the Maxwell model on a sheet, with particular emphasis on melting heat and zero mass flux at the boundary, as motivated by both the Cattaneo–Christov heat flux and the Lorentz force-based (TMS-MHZCL) models. This study presents four unique scenarios of the TMS-MHZCL model, focusing on the velocity and temperature profiles, as illustrated in Table 3.

Table 3. Fluctuations in physical parameters of TMS-MHZCL model.

S=Scenario, C=Case	M	M_e	β	Pr
S1/C1	0.0	0.5	0.2	3.0
S1/C2	0.5	0.5	0.2	3.0
S1/C3	1.0	0.5	0.2	3.0
S1/C4	1.5	0.5	0.2	3.0
S1/C5	2.0	0.5	0.2	3.0
S2/C1	1.0	0.0	0.2	3.0
S2/C2	1.0	0.5	0.2	3.0
S2/C3	1.0	1.0	0.2	3.0
S2/C4	1.0	1.5	0.2	3.0
S2/C5	1.0	2.0	0.2	3.0
S3/C1	1.0	0.5	0.0	3.0
S3/C2	1.0	0.5	0.2	3.0
S3/C3	1.0	0.5	0.5	3.0
S3/C4	1.0	0.5	0.8	3.0
S3/C5	1.0	0.5	1.0	3.0
S4/C1	1.0	0.5	0.2	1.0
S4/C2	1.0	0.5	0.2	2.0
S4/C3	1.0	0.5	0.2	3.0
S4/C4	1.0	0.5	0.2	4.0
S4/C5	1.0	0.5	0.2	5.0

Four different scenarios have been identified utilizing the LSRNNs-LMO approach on the TMS-MHZCL model. This section also provides an in-depth overview of the outcomes obtained from applying the LSRNN-LMO technique. The assessment and interpretation component is essential to our research on LSRNNs-LMO, given its rigorous structure and data analysis. The proposed methodology elucidates the complexities of heat transfer, chemical reaction kinetics, and fluid dynamics, providing a foundation for a comprehensive study that yields precise predictions across diverse physical domains.

Maxwell fluids are crucial to numerous industries and biological processes due to their simultaneous viscous and elastic properties. The LSRNNs-LMO scheme has not been utilized to examine the TMS-MHZCL model. We applied the AI-driven LSRNNs-LMO scheme to TMS-MHZCL model. Figures 3–8 illustrate the LSRNNs-LMO solutions for each of the four scenarios, which encompass various circumstances as evaluated through performance metrics, mean square error, fitness functions, histogram graphs, input-error cross-correlation, and regression analysis. Tables 1 and 2 present the results of the LSRNNs-LMO approach using the metrics MSE, RMSE, MAE, MAPE, NSE, and R^2 for the TMS-MHZCL model.

Figure 3 demonstrates the learning behavior (training state) of LSRNNs-LMO technique for the TMS-MHZCL model. Figures 3(a)–(d) highlights the best gradient values of 7.65×10^{-5}, 2.16×10^{-4}, 2.4×10^{-7}, and 4.08×10^{-8} across four different scenarios of the first case. The computed gradients validate the consistency and validity of the proposed LSRNNs-LMO technique.

The MSE and RMSE are widely recognized metrics for model assessment. These metrics have been adopted as standard statistical measures to analyze the performance efficiency of the LSRNNs-LMO approach for the TMS-MHZCL model. MSE is a primary measure of model accuracy and is widely used as a comprehensive reference criterion, with smaller values near zero preferred. RMSE is another essential metric for quantifying the deviation between the estimator's predictions and the actual values.

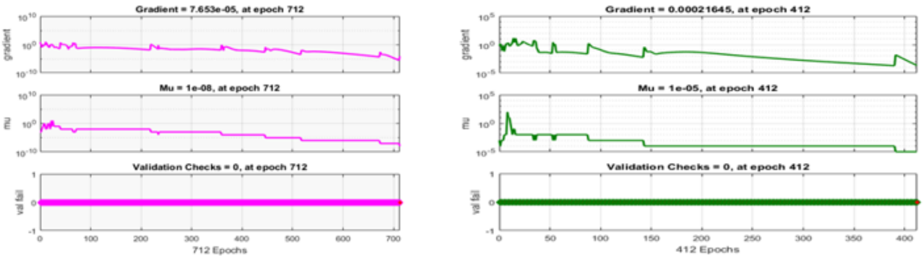

(a) Training State (TS) of SI/C1.

(b) Training State (TS) of SII/C1.

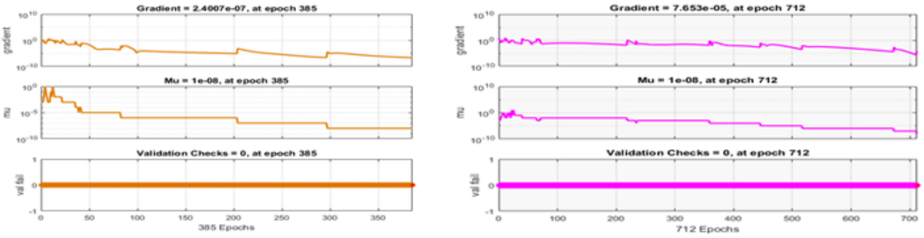

(c) Training State (TS) of SIII/C1.

(d) Training State (TS) of SIV/C1.

Figure 3. Learning-based training state (TS) configuration of LSRNNS-LMO for the TMS-MZCL model.

A lower MSE signifies improved optimization performance. The optimal MSE training results are shown in Figure 4. Figures 4(a)–(d) presents the best MSE values of 2.25×10^{-13}, 1.71×10^{-11}, 3.77×10^{-13}, and 7.71×10^{-10} across four different scenarios of the first case. These minimal and decreasing MSE trends confirm the robustness and stability of the proposed model. Likewise, the optimal RMSE values 4.74×10^{-7}, 4.14×10^{-6}, 6.14×10^{-7}, and 2.77×10^{-5} obtained for the same cases, further indicate the effectiveness of the proposed scheme. These outcomes collectively reflect a high degree of computational precision.

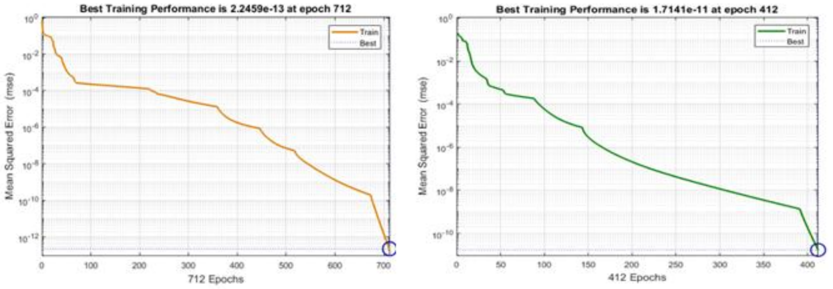

(a) Optimization control curves for SI\CI.

(b) Optimization control curves for SII\CI.

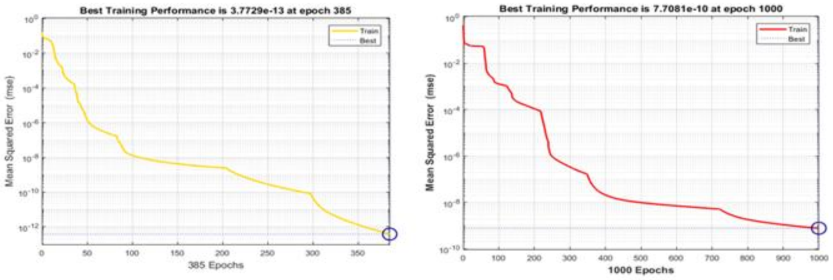

(c) Optimization control curves for SIII\CI.

(d) Optimization control curves for SIV\CI.

Figure 4. Fitness-based MSE optimization using a configuration of LSRNNs-LMO for the TMS-MHZCL model.

Figure 5 illustrates the input-error cross-correlation analysis, which further validates network performance by investigating the correlation between the input sequence and corresponding errors. The observed association suggests that increasing the number of lag terms in the tapped-delay lines may enhance prediction accuracy. In an ideal predictive framework, all correlations should approach zero. If the input shows a relationship with the error, improving prediction performance can be achieved by increasing the number of delay elements in the connected layers. In this study, nearly all correlations remain within the confidence limits around zero. Figure 6 presents the error autocorrelation function, which evaluates the performance of the developed network by illustrating the temporal relationships of forecasting errors. Autocorrelation analysis of errors is employed to examine the interrelationships between inputs and prediction errors by including multiple lag terms. A noticeable correlation was observed in the forecasting errors, with most trained networks lying within the red confidence limits, signifying potential for improvement, possibly by increasing the number of neurons or delay elements. When the network is trained correctly, the remaining lines become significantly shorter; otherwise, they remain confined within the red confidence intervals.

For an ideal forecasting model, there must be a singular nonzero value of the autocorrelation function, which should manifest at zero latency (the mean squared error). This would imply that the forecasting errors were entirely independent of one another (white noise). If a strong correlation exists in the forecasting errors, it may be feasible to improve the estimation, potentially by increasing the number of lags in the tapping-delaying lines. In this instance, the correlations, except the one at zero lag, predominantly lie within the 95% confidence intervals around zero, indicating that the model appears satisfactory.

Figures 5 and 6 highlight the efficiency and coherence of the proposed LSRNNs-LMO technique by showing correlations across all four cases that remain within the confidence limits and converge toward the zero reference point.

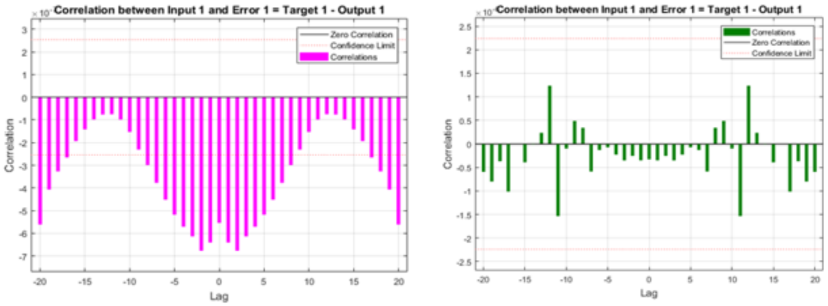

(a) Input cross-correlation for SI/CI.

(b) Input cross-correlation for SII/CI.

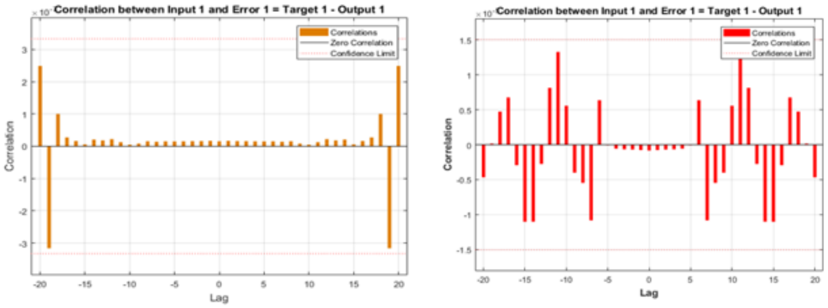

(c) Input cross-correlation for SIII/CI.

(d) Input cross-correlation for SIV/CI.

Figure 5. Evaluations of the efficacy of LSRNNs-LMO for the TMS-MHZCL model.

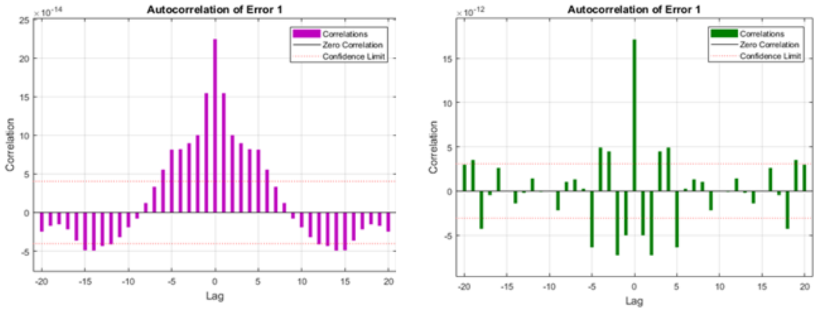

(a) Auto-correlation of errors for SI/CI.

(b) Auto-correlation of errors for SII/CI.

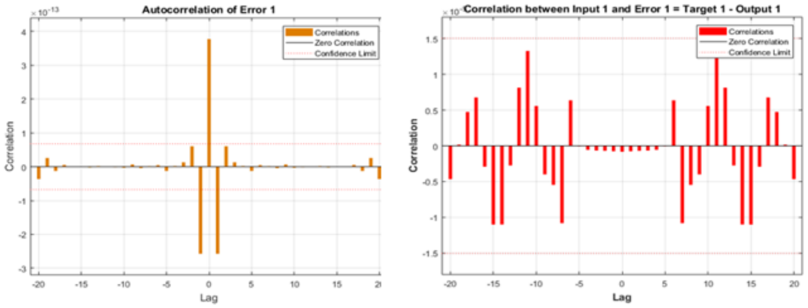

(c) Auto-correlation of errors for SIII/CI.

(d) Auto-correlation of errors for SIV/CI.

Figure 6. Evaluation of the LSRNNs-LMO results' suitability for the TMS-MHZCL model.

Figure 7 presents an error histogram illustrating a normal distribution of errors. The histogram has 20 bins, symmetrically distributed across the positive and negative ranges. This graphical representation aids in detecting outliers in the dataset, where outliers correspond to data points that exhibit a significantly poorer fit than the other data points. The errors close to zero are 2.8×10^{-8}, -1, 2×10^{-6}, -2.9×10^{-7}, and -4.5×10^{-6}, which validate the reliability of the network. These negligible errors further confirm the stability and efficiency of the proposed scheme.

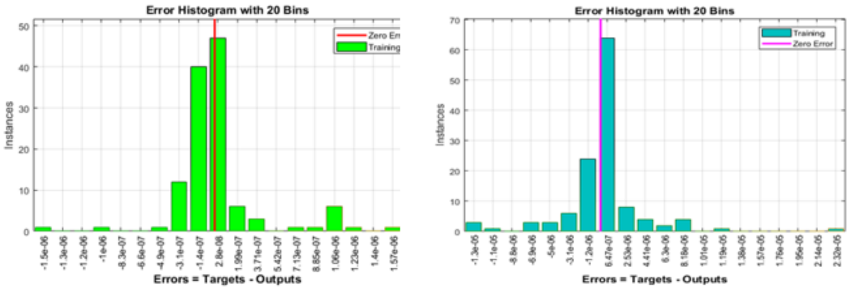

(a) Error Histogram for SI/CII.

(b) Error Histogram for SII/CII.

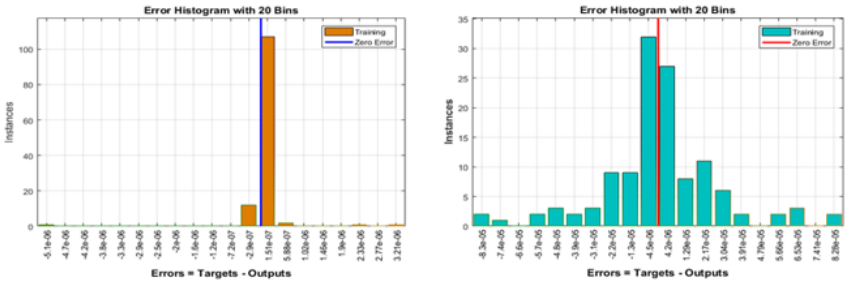

(c) Error Histogram for SIII/CII.

(d) Error Histogram for SIV/CII.

Figure 7. Evaluation of the error histogram to demonstrate the LSRNNs-LMO results' suitability for the TMS-MHZCL model.

In regression analysis, the primary focus is on assessing how well the data fit the model. When the data points coincide with the linear target line, the curve fitting is considered optimal. A higher R^2 value indicates that the data points align more closely with the regression line, reflecting a stronger correlation between the predicted and actual values. A coefficient of variation equal to 1 indicates that the total variability in the dependent variable is entirely due to the independent variable, confirming ideal curve fitting. Conversely, an R^2 value approaching zero denotes the failure of the linear relationship between the targets and outputs, whereas an R^2 value equal to 1 represents a perfect linear association. Furthermore, Figure 8 presents the regression analysis, which shows that all data points lie precisely along the solid regression line, confirming the best-fit model.

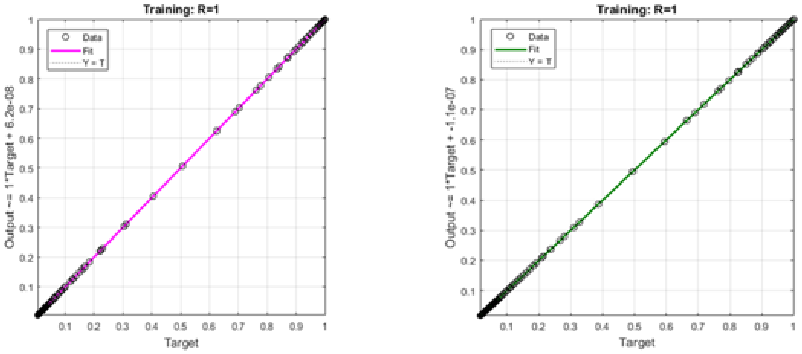

(a) Regression analysis for SI/CII.

(b) Regression analysis for SII/CII.

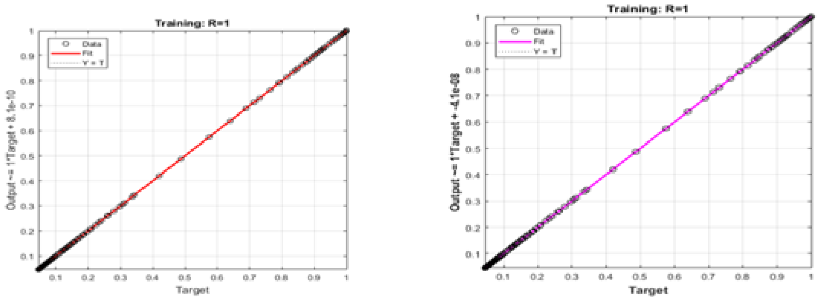

(c) Regression analysis for SIII/CII.

(d) Regression analysis for SIV/CII.

Figure 8. Evaluation of the regression analysis to demonstrate the LSRNNs-LMO results' suitability for the TMS-MHZCL model.

Our work investigates the steady-state flow of Maxwell fluids over a sheet-shaped domain, focusing specifically on the influence of the melting temperature and the zero-mass-flux boundary condition. A Maxwell fluid, distinguished by its viscosity and elasticity properties, is essential in numerous industrial and biological applications. Our investigation of the TMS-MHZCL flow over a stretching sheet yields valuable insights into the thermal transfer properties of nanofluids. The LSRNN-LMO algorithm demonstrated exceptional accuracy, with error margins as minimal as 10^{-9}. These results include significant practical ramifications for numerous enterprises. In the electronic refrigeration sector, the enhanced thermal properties of nanofluids can optimize liquid radiators for exceptional durability in data centers and computing centers. Our methodology in healthcare engineering can facilitate the development of microfluidic devices for efficient drug delivery. Moreover, integrating nanofluids into automotive cooling systems enhances engine heat management, while advancements in renewable energy can improve the effectiveness of solar thermal collectors. This research advances a theoretical understanding and identifies practical opportunities to enhance sustainability and effectiveness across sectors.

Figure 9(a) illustrates the effect of the MHD parameter on the velocity profile. As the MHD parameter escalates, the velocity profile diminishes. The physical mechanism depicted in Figure 9(a), in which an increased MHD value leads to a reduced velocity profile, arises from the interaction between the magnetic field and fluid motion. This decline is primarily determined by the interaction between parameter M and the complexity of the fluid flow. The magnetic field exerts stress on the fluid, thereby restricting or weakening its motion. Increasing the MHD value, often indicative of a stronger magnetic field, may yield several outcomes. The magnetic field generates a Lorentz force on the charged particles within the fluid. This force may accelerate or oppose the fluid flow, depending on the direction of M and the orientation of the fluid's current. The magnetic field can induce magnetic tension in the fluid, thereby constraining or attenuating the flow. Intense magnetic forces can suppress fluid turbulence, and reducing these effects promotes a more orderly, stable flow, consequently diminishing the velocity profile, since turbulence generally enhances mixing and transport processes. The observed behavior may vary depending on the system geometry, fluid properties, and the M parameter. In certain instances, an elevated MHD parameter may improve the velocity profile, particularly when the magnetic field is designed to promote flow; however, in many scenarios, increasing the MHD parameter generally diminishes the velocity contours due to the effects described above. Figure 9(b) presents the absolute error for the variation for the M parameter of the velocity profile, showing approximately 10^{-8} minimal error. Figure 9(c) depicts the effect of melting heat (M_e) stimulation on the velocity profile, where a noticeable increase in velocity is observed with rising (M_e) influence. The physical structure underlying the behavior shown in Figure 9(c), in which an escalating M_e corresponds to an enhanced velocity profile, pertains to the latent heat of melting and its impact on fluid dynamics, particularly in phase-change phenomena. The stronger melting supplies additional liquid and latent heat at the interface, thereby weakening viscous resistance and accelerating the fluid adjacent to the melting surface. Figure 9(d) shows the absolute error for variations in the M_e parameter of the velocity profile, exhibiting a negligible error close to 10^{-8}. Figure 9(e) demonstrates the influence of the MHD parameter (M) on the temperature distribution, where the temperature profile displays a declining trend with increasing MHD intensity. The underlying physical mechanism shown in Figure 9(e) indicates that an increasing MHD factor leads to a decline in the temperature profile, which is fundamentally linked to the correlation between M and the fluid's thermal characteristics. An increase in MHD parameter (M) typically indicates that the conducting fluid is exposed to a stronger magnetic field.

An increase in MHD parameter (M) usually signifies a higher magnetic field produced by the conductive fluid. The magnetic field present exerts forces on charged particles in the liquid, resulting in the manifestation of the Lorentz force. These forces may subsequently result in magnetic restriction or a compression of fluid in certain areas. As the magnetic field increasingly confines the fluid, it may undergo reduced expansion due to heat, resulting in lower temperatures in those regions. The presence of a robust MHD parameter (M) can impede heat conduction and transmission within the fluid. This aids in the comprehensive decrease of the temperature profile. In certain instances, the relationship between the MHD parameter (M) and the fluid can generate Alfven waves that transport energy through the fluid. These electromagnetic waves may redistribute energy within the system, resulting in temperature variations that frequently reduce the temperature contour.

Figure 9(f) illustrates the absolute error associated with the variation of the M parameter along the temperature profile, showing a negligible deviation of approximately 10^{-7}. Figure 9(g) shows the influence of melting heat (M_e) on the temperature profile, highlighting the evident interdependence between the two parameters. A noticeable drop in the temperature profile occurs as the influence of melting heat becomes more dominant. This phenomenon arises from the fundamental principles of thermodynamics that govern phase transitions, particularly the release of latent heat during the solid-to-liquid transition. The escalation of the melting heat (M_e) indicates a greater quantity of thermal energy being released during the phase change from solid to liquid. As the substance melts, more heat is released into the surrounding atmosphere. The expulsion of heat cools the surrounding area, as the emitted heat extracts energy from the adjacent fluid or material, thereby lowering the temperature. The more substantial melting at the surface is indicated by a larger melting parameter, whereby more solid transforms into liquid. During melting, latent heat is absorbed at the interface, extracting energy from the nearby fluid and thus lowering its temperature. Moreover, the fluid temperature within the boundary layer decreases with increasing of melting heat (M_e), although all profiles eventually approach the ambient temperature far from the surface. Figure 9(h) displays the absolute error curve for the variation of the M_e parameter with respect to the temperature profile, exhibiting a minimal deviation of approximately 10^{-8}. Figure 9(i) demonstrates the effect of the β parameter on the temperature distribution. The temperature profile shows a significant rise as the β parameter increases. The physical mechanism illustrated in Figure 9(i), in which a growing β factor produces an elevated temperature profile, relates to the viscoelastic properties of materials and their response to temporal thermal variations. A higher β parameter value implies that the elastic response of the material dominates over its viscous behavior. The higher β reflects the stronger elastic contribution relative to viscous effects in the fluid interaction response. This enhanced elasticity enables the medium to store and release more thermal energy, thereby diminishing the rate of heat diffusion away from the heated surface. The elevated β factor indicates a rapid, dominant elastic response from the material. The material can exhibit more pronounced temperature fluctuations and an overall increase in the temperature profile if it can quickly regulate its temperature in response to thermal gradients. Figure 9(j) illustrates the absolute error associated with variations in the β parameter concerning the temperature profile, indicating minimal discrepancies on the order of 10^{-9}. Figure 9(k) shows the complex correlation between the Prandtl number (Pr) and the temperature profile, revealing a significant link among these factors. A noticeable rise in the temperature trend is observed as the Pr number increases. The governing mechanism for this phenomenon, depicted in Figure 9(k), where an increasing Pr number corresponds to higher temperature behavior, arises from the intricate coupling of heat transfer processes with varying momentum and heat diffusion characteristics in the fluid. An increase in the Pr number indicates the fluid's performance in momentum transmission relative to its capability in heat transfer. A greater Pr value indicates that the fluid is less efficient in momentum transfer compared to its proficiency in heat transport. The discrepancies signify that thermal diffusion occurs at a faster rate than momentum diffusion inside the fluid. Consequently, as the Pr number increases, the fluid has an enhanced ability to mix and transfer heat effectively. As the Pr number rises, the fluid's improved capacity for heat transmission becomes evident, leading to a rise in the temperature profile. The intricate relationship between the Prandtl number and temperature dynamics highlights the crucial influence of heat transfer properties and the varying rates of momentum and thermal diffusion in defining the thermal behavior of fluids. This complex interaction demonstrates that an increasing Prandtl number enhances the efficiency of thermal energy transfer, leading to a significant increase in the system's temperature profile. Figure 9(l) depicts the absolute error corresponding to the variation of the Pr number on the temperature profile. It indicates minimal errors within the range of 10^{-9} for the given temperature profile. Furthermore, Figure 9 presents the comparison results for the proposed scheme, which closely match the numerical outcomes and exhibit minimal absolute errors.

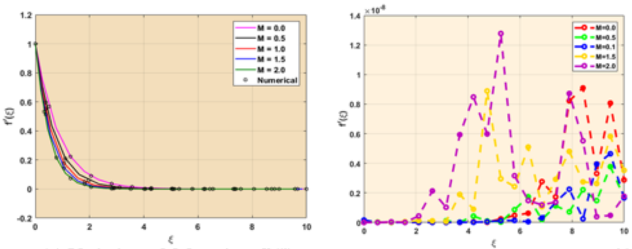

(a) Variation of M against $f'(\xi)$. (b) Absolute error for M against $f'(\xi)$.

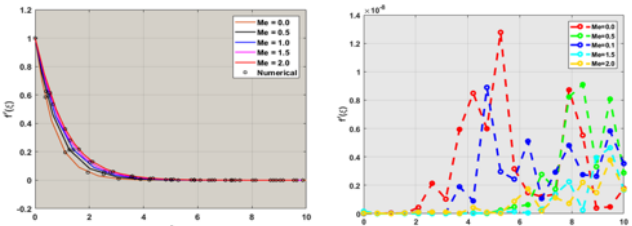

(c) Variation of M_e against $f'(\xi)$. (d) Absolute error for M_e against $f'(\xi)$.

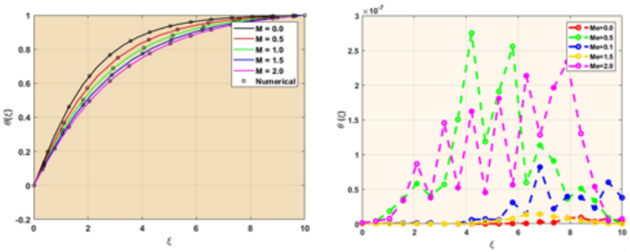

(e) Variation of M against $\theta(\xi)$. (f) Absolute error for M against $\theta(\xi)$.

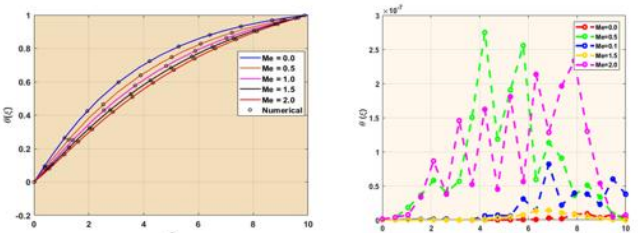

(g) Variation of M_e against $\theta(\xi)$. (h) Absolute error for M_e against $\theta(\xi)$.

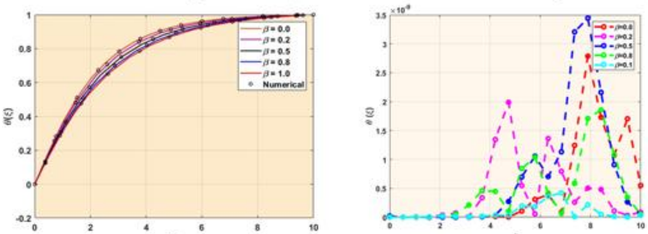

(i) Variation of β against $\theta(\xi)$. (j) Absolute error for β against $\theta(\xi)$.

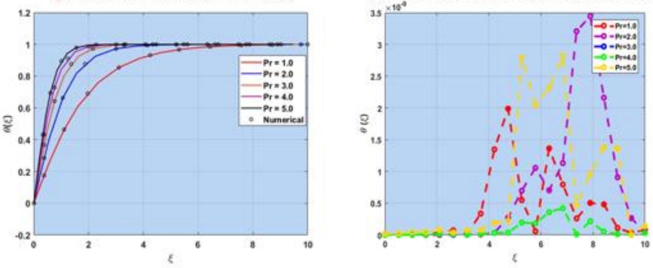

(k) Variation of Pr against $\theta(\xi)$. (l) Absolute error of Pr against $\theta(\xi)$.

Figure 9. Comparative outcomes and assessments of the LSRNNs-LMO model with $f'(\xi)$ and $\theta(\xi)$ based on the reference dataset of the TMS-MHZCL model.

5. Conclusions

This article presents a novel methodology to investigate the thermodynamic properties of the Maxwell model on a sheet, with particular focus on melting heat and zero-mass-flux boundary conditions, inspired by the Cattaneo-Christov heat flux formulation and the Lorentz force effects (TMS-MHZCL) model, and employing advanced computational approaches. Maxwell fluids are crucial in a variety of scientific and biological applications owing to their unique combination of viscous and elastic properties. A soft computational LSRNN-LMO technique is designed and implemented for forecasting the TMS-MHZCL flow. Maxwell fluids are crucial across numerous economic and biomedical domains due to their distinctive viscoelastic properties. The TMS-MHZCL model demonstrates applicability in scientific and industrial settings, particularly for enhancing heat-transfer processes. The present work identifies numerical solutions using a sophisticated computational method. Temperature, velocity, and many physical parameters are delineated, and their effects are comprehensively analyzed using diverse graphical representations. The current study has produced significant results, presented as follows:

- The investigation demonstrates the application of modern AI innovations, particularly LSRNNs-LMO, to analyzing the TMS-MHZCL model.
- The proposed technique aims to achieve optimal outcomes and compare them with experimental numerical findings to validate their precision within a small error margin.
- A graphical depiction of the outcomes obtained by the sophisticated, AI-powered application of the LSRNNs-LMO technique is shown via a comparison analysis. Regression graphs, correlation plots, error histograms, and error auto-regression analyses were employed to confirm the effectiveness of measurement and comparison studies utilizing NSLRNNs.
- The regression analysis, yielding a value close to 1, signifies the reliability and effectiveness of the proposed technique.
- As the MHD factor M escalates, a notable decrease in the velocity profile is observed, signifying a fall in the fluid's velocity.
- The temperature profile diminishes as the MHD factor M grows, signifying a declining tendency in the system’s distribution of temperatures.
- The velocity profile notably rises with the amplification of the melting heat action. The physical concepts related to the latent heat of melting and its influence on fluid dynamics, particularly during phase transition processes, explain the occurrence.
- As the β parameter increases, the temperature profile significantly decreases. An increased β factor value results in a stronger temperature dependence and is linked to the elastic properties of materials and their responses to temporal changes in temperature.
- An evident escalation in the temperature trend occurs as the $\Pr$ number increases.

Limitations of the proposed technique and future work

The integration of layered supervised recurrent neural networks with the Levenberg-Marquardt optimization (LSRNNs-LMO) technique in fluid mechanics holds considerable promise for complex simulations and time-varying flow phenomena; yet, many limitations persist. A significant limitation of the employed LSRNNs-LMO methodology is its reliance on highly specialized training data to capture essential physical correlations and to produce accurate predictions. Incomplete or insufficient datasets can lead to diminished model reliability and erroneous predictions. Furthermore, LSRNN-LMO is highly sensitive to hyperparameter settings, and inappropriate settings may lead to overfitting or convergence issues. There exist auspicious prospects for forthcoming research in fluid mechanics. Sophisticated investigations, including those that leverage RNNs and computational power [18,19], have yielded promising results and facilitated the practical analysis of complex events. Advanced machine architectures employing artificial recurrent neural networks are being developed to analyze and better understand various fluid flow systems [20,21]. The extension of neural networks into multiple domains and the transdisciplinary challenges they pose are notably promising. By employing RNNs across domains, researchers can examine the complexities of social issues, propose novel concepts, and devise innovative solutions. As a result, the effort will foster collaboration and innovation that may lead to significant advances in technological and scientific fields.

Author contributions

Sana Ullah Saqib: Writing original draft, investigation, software, methodology, formal analysis, data curation; Yin-Tzer Shih: Writing review & editing, conceptualization, supervision; Muhammad Jahanzaib: Software, investigation, visualization; Abdul Wahab: Software, investigation, visualization, validations; Adnan: Software, investigation, visualization; Shih-Hau Fang: Methodology, software, investigation. All authors have read and approved the final version of the manuscript for publication.

Use of Generative-AI tools declaration

The authors declare that they have not used any artificial intelligence (AI) tools in creating this article.

Acknowledgments

The authors thank the anonymous referees for their constructive comments and valuable suggestions. The first, second, and third authors gratefully acknowledge the support of the National Science and Technology Council (NSTC), Taiwan, through the NSTC project under Grant No. NSTC 114-2115-M-005-002-MY2. The last author acknowledges the support of the National Science and Technology Council (NSTC), Taiwan, under Grant No. NSTC 114-2634-F-001-003.

Conflict of interest

The authors declare that they have no known competing financial interests or personal relationships that could have appeared to influence the work reported in this paper.

References

1. D. H. Zhou, Z. Y. Song, Z. C. Chen, X. T. Huang, C. M. Ji, S. Kumari, et al., Advancing explainability of adversarial trained convolutional neural networks for robust engineering applications., *Eng. Appl. Artif. Intel.*, **140** (2025), 109681. https://doi.org/10.1016/j.engappai.2024.109681

2. U. Farooq, S. U. Saqib, S. A. Khan, H. H. Liu, N. Fatima, T. Muhammad, et al., Mathematical modeling of radiative nanofluid flow over nonlinear stretching sheet using artificial neural networks and Levenberg-Marquardt scheme: Applications in solar thermal energy, *Sol. Energ. Mat. Sol. C.*, **281** (2025), 113265. https://doi.org/10.1016/j.solmat.2024.113265
3. O. Orojo, J. Tepper, T. M. McGinnity, M. Mahmud, The multi-recurrent neural network for state-of-the-art time-series processing, *Procedia Computer Science*, **222** (2023), 488–498. https://doi.org/10.1016/j.procs.2023.08.187
4. A. Nishihata, O. Tonomura, K. I. Sotowa, Accelerating unsteady fluid dynamic simulations for microdevices for Droplet generation using singular value decomposition and recurrent neural network, *Chemical Engineering Transactions*, **118** (2025), 439–444. https://doi.org/10.3303/CET25118074
5. M. Khan, M. Imran, W. Khan, A neural network approach to modeling magnetohydrodynamic stagnation point Ree-Eyring flow over a convectively heated stretched surface, *International Journal of Modelling and Simulation*, **2024** (2024), 2338579. https://doi.org/10.1080/02286203.2024.2338579
6. S. U. Saqib, U. Farooq, N. Fatima, Y.-T. Shih, A. Mir, L. Kolsi, Novel Recurrent neural networks for efficient heat transfer analysis in radiative moving porous triangular fin with heat generation, *Case Stud. Therm. Eng.*, **64** (2024), 105516. https://doi.org/10.1016/j.csite.2024.105516
7. M. B. Jeelani, A. Abbas, Thermal efficiency of spherical nanoparticles Al2O3-Cu dispersion in ethylene glycol via the MHD non-Newtonian Maxwell fluid model past the stretching inclined sheet with suction effects in a porous space, *Processes*, **11** (2023), 2842. https://doi.org/10.3390/pr11102842
8. N. Venkatesh, R. S. Raju, M. A. Kumar, C. Vijayabhaskar, Heat and mass transfer in Maxwell fluid with nanoparticles past a stretching sheet in the existence of thermal radiation and chemical reaction, *International Journal of Modelling and Simulation*, **45** (2025), 1200–1213. https://doi.org/10.1080/02286203.2023.2266798
9. J. F. Cui, F. Azam, U. Farooq, M. Hussain, Non-similar thermal transport analysis in entropy optimized magnetic nanofluids flow by considering effective Prandtl number model with melting heat transfer and Joule heating, *J. Magn. Magn. Mater.*, **567** (2023), 170331. https://doi.org/10.1016/j.jmmm.2022.170331
10. M. Khan, Z. D. Zhang, D. C. Lu, Numerical simulations and modeling of MHD boundary layer flow and heat transfer dynamics in Darcy-forchheimer media with distributed fractional-order derivatives, *Case Stud. Therm. Eng.*, **49** (2023), 103234. https://doi.org/10.1016/j.csite.2023.103234
11. M. Khan, A. Alhowaity, M. Imran, M. Hussien, R. Alroobaea, M. S. Anwar, Advanced numerical simulation techniques in MHD fluid flow analysis using distributed fractional order derivatives and Cattaneo heat flux model, *ZAMM-Z. Angew. Math. Me.*, **104** (2024), e202300622. https://doi.org/10.1002/zamm.202300622
12. M. S. Anwar, T. Muhammad, M. Khan, V. Puneeth, MHD nanofluid flow through Darcy medium with thermal radiation and heat source, *Int. J. Mod. Phy. B*, **38** (2024), 2450386. https://doi.org/10.1142/S0217979224503867
13. M. S. Anwar, M. Khan, Z. Hussain, T. Muhammad, V. Puneeth, Investigation of heat transfer characteristics in MHD hybrid nanofluids with variable viscosity and thermal radiations, *J. Radiat. Res. Appl. Sc.*, **18** (2025), 101240. https://doi.org/10.1016/j.jrras.2024.101240

14. B. Jalili, A. Rezaeian, P. Jalili, F. Ommi, D. D. Ganji, Numerical modeling of magnetic field impact on the thermal behavior of a microchannel heat sink, *Case Stud. Therm. Eng.*, **45** (2023), 102944. https://doi.org/10.1016/j.csite.2023.102944
15. N. A. Yacob, A. Ishak, I. Pop, Melting heat transfer in boundary layer stagnation-point flow towards a stretching/shrinking sheet in a micropolar fluid, *Comput. Fluids*, **47** (2011), 16–21. https://doi.org/10.1016/j.compfluid.2011.01.040
16. A. Ramar, A. Arulmozhi, S. Balamuralitharan, I. Khan, F. Hajjej, M. A. Khuthaylah, et al., Melting heat effect in MHD flow of maxwell fluid with zero mass flux, *Case Stud. Therm. Eng.*, **53** (2024), 103910. https://doi.org/10.1016/j.csite.2023.103910
17. R. G. Abdel-Rahman, M. M. Khader, A. M. Megahed, Melting phenomenon in magneto hydro-dynamics steady flow and heat transfer over a moving surface in the presence of thermal radiation, *Chinese Phys. B*, **22** (2013), 030202. https://doi.org/10.1088/1674-1056/22/3/030202
18. U. Farooq, S. A. Khan, H. H. Liu, M. Imran, L. B. Said, A. Ramzan, et al., Application of artificial intelligence brain structure-based paradigm to predict the slip condition impact on magnetized thermal Casson viscoplastic fluid model under combined temperature dependent viscosity and thermal conductivity, *Case Stud. Therm. Eng.*, **66** (2025), 105702. https://doi.org/10.1016/j.csite.2024.105702
19. S. A. Khan, U. Farooq, M. Imran, H. H. Liu, T. Muhammad, M. Alghamdi, Mathematical and artificial neural network modeling to predict the heat transfer of mixed convective electroosmotic nanofluid flow with Helmholtz-Smoluchowski velocity and multiple slip effects: an application of soft computing, *Case Stud. Therm. Eng.*, **61** (2024), 104950. https://doi.org/10.1016/j.csite.2024.104950
20. M. Hussain, D. Lin, H. Waqas, F. Jiang, T. Muhammad, Advanced thermal performance of blood-integrated tri-hybrid nanofluid: an artificial neural network-based modeling and simulation, *Mech. Time-Depend. Mater.*, **29** (2025), 16. https://doi.org/10.1007/s11043-024-09748-7
21. A. S. Alnahdi, T. Gul, Neural network analysis for prediction of heat transfer of aqueous hybrid nanofluid flow in a variable porous space with varying film thickness over a stretched surface, *Chinese Phys. B*, **34** (2025), 024701. https://doi.org/10.1088/1674-1056/ad989c